metals

Article

Precipitation Behavior and Corrosion Properties of Stirred Zone in FSWed AA5083 Al-Mg Alloy after Sensitization

Wenbin Gao [1,2], Jiaao Ning [3], Xiaoyan Gu [4], Liangyu Chen [1,*], Hang Liang [3,*], Wenhang Li [1] and John J. Lewandowski [5]

1 Department of Materials Science and Engineering, Jiangsu University of Science and Technology, Zhenjiang 212000, China; gaowb@just.edu.cn (W.G.); lwh_jkl@just.edu.cn (W.L.)
2 Foshan (Southern China) Institute for New Materials, Foshan 528200, China
3 Department of Materials Science and Engineering, Tianjin University, Tianjin 300350, China; nja86882077@163.com
4 Department of Materials Science and Engineering, Hubei University of Automotive Technology, Shiyan 442002, China; liligu1983@163.com
5 Department of Materials Science and Engineering, Case Western Reserve University, Cleveland, OH 44106, USA; jjl3@case.edu
* Correspondence: lychen@just.edu.cn (L.C.); hangliang@tju.edu.cn (H.L.)

Abstract: This paper investigated the Mg-rich phase precipitation behavior and the corrosion performance throughout the thickness direction within the stirred zone (SZ) of friction stir welded (FSW) AA5083 alloy after 175 °C/100 h sensitization. For the as-welded SZ, the recrystallized grain size gradually decreased from the top surface (5.5 μm) to the bottom (3.7 μm). The top and bottom of the SZ maintained relatively high levels of deformed grains and accumulated strain induced by either shoulder pressing or pin stirring. After 175 °C/100 h sensitization, 100 nm thick β'-Al_3Mg_2 precipitates were present along the grain boundaries (GBs) in the SZ. The bottom of the SZ exhibited more continuous precipitates along GBs due to the fine grain size and the large fraction of high-angle grain boundaries (0.724%). Although the as-welded SZ exhibited excellent corrosion resistance, it became extremely vulnerable to intergranular cracking (IGC) and stress corrosion cracking (SCC) after sensitization. The large SCC susceptibility indices of the SZ samples ranged from 66.9% to 73.1%. These findings suggest that sensitization can strongly deteriorate the corrosion resistance of the Al-Mg FSW joint, which is of critical importance for the safety and reliability of marine applications.

Keywords: Al-Mg alloy; friction stir welding; Mg-rich phase; sensitization; stress corrosion cracking

Citation: Gao, W.; Ning, J.; Gu, X.; Chen, L.; Liang, H.; Li, W.; Lewandowski, J.J. Precipitation Behavior and Corrosion Properties of Stirred Zone in FSWed AA5083 Al-Mg Alloy after Sensitization. *Metals* **2023**, *13*, 1618. https://doi.org/10.3390/met13091618

Academic Editor: Babak Shalchi Amirkhiz

Received: 17 August 2023
Revised: 15 September 2023
Accepted: 16 September 2023
Published: 19 September 2023

1. Introduction

The 5xxx series aluminum–magnesium alloys are widely concerned and employed in shipbuilding, aerospace, and industry manufacturing by virtue of their excellent toughness, weldability, strength-to-weight ratio, and corrosion resistance [1–4]. These Al-Mg alloys are generally regarded as the predominant alternative to steel structures [5]. However, many studies have provided sufficient evidence that when Al-Mg alloy structures are exposed to a specific temperature range (40–200 °C) for an extent of time, the electrochemically active Al_3Mg_2 phases may precipitate along the grain boundaries and trigger severe intergranular corrosion (IGC) and stress corrosion cracking (SCC) [6–9]. Mg-rich phase nucleation and growth behavior have been investigated in detail for decades, and factors affecting Mg-rich phase precipitation behavior mainly include grain structures [10,11], grain boundary characteristics [12–14], dislocation density [15,16], and the combinations of suffered temperature and exposed time [17–19]. The SCC mechanism of sensitized Al-Mg alloys has been studied extensively, and most studies have suggested two cases of "anodic dissolution" [20,21] and/or "hydrogen-enhanced decohesion embrittlement" (HEDE) [22–24]. In both cases, the continuously distributed or near-spaced Mg-rich phase along the grain boundaries (GBs) is the prerequisite for subsequent IGC or SCC.

Friction stir welding (FSW), a solid-state welding technique, has been frequently applied in joining Al-Mg alloys. Excellent mechanical properties can be obtained, and the solidification defects, such as pores and hot cracks, observed in the traditional fusion welding processes can be effectively avoided via dynamic recrystallization [25–28]. In recent years, studies have been conducted on the Mg-rich phase precipitation behavior of FSWed Al-Mg alloys [29–31], and FSW was adopted as a reverse heat treatment aiming to eliminate sensitization [32]. Our previous work demonstrated that the thermal–mechanical affected zone (TMAZ) and the stirred zone (SZ) exhibited more severe IGC/SCC susceptibility compared with the base metal [29]. The large corrosion tendency exhibited in the SZ after sensitization was also confirmed by Qiu's work via potentiodynamic polarization curves and NAMLT tests [31]. The majority of these aforementioned studies have focused on Al-Mg alloy plates with a thickness of less than 10 mm. However, thick Al-Mg alloy plates are increasingly utilized in marine structures to satisfy the requirements of service in complicated conditions. There is little published information on the variation of the Mg-rich precipitates and IGC/SCC behavior throughout the thickness of the Al-Mg alloy, especially for Al-Mg FSW joints. At present, there exists limited research about the microstructure–property relationships and deformation characteristics at various through-thickness locations of the FSWed thick plate [33–35]. Previous studies have found that the grain size decreased and the dislocation density increased from the top to the bottom in the SZ of the thick AA5083 FSW joint [36].

The existing studies on thick Al-Mg FSW joints have mainly focused on microstructures and mechanical responses. To the authors' best knowledge, a systematic understanding of the sensitization behavior targeting thick Al-Mg alloy plate FSW joints is still lacking. The microstructure inhomogeneity of SZ due to the non-uniform heat and plastic deformation throughout the thickness will inevitably affect the Mg-rich phase precipitation and the subsequent corrosion behavior. However, few scholars have been able to draw on any systematic research into these aspects. An understanding of the sensitization behavior of Al-Mg welds is still required for further support.

In this study, 12-mm-thick FSWed Al-Mg alloy sheets were investigated, aiming to fully analyze the relationship between the through-thickness microstructural characteristics and the Mg-rich phase precipitation behavior within the stirred zone. The IGC and SCC susceptibilities throughout the thickness direction were also comprehensively investigated. The results of this study serve to highlight the importance of understanding the IGC/SCC tendency of Al-Mg marine structures during service. Additional research is also necessary to mitigate the damage caused by sensitization.

2. Materials and Methods

2.1. Material and Welding Process

The chemical composition of AA5083-H112 Al-Mg alloy studied herein is listed in Table 1, and the thickness of the alloy sheet was 12 mm. Defect-free FSW joints were obtained utilizing a gantry welding machine. The oxidation films were removed with a wire brush, and then the plate surfaces were rinsed with ethanol prior to the welding experiments. The diameter of the left-hand threaded pin was 12.8 mm for the top and 8 mm for the bottom. The tool rotation speed was 300 rpm, and the traveling speed was 50 mm/min. The stir pin was penetrated to a depth of 12 mm and was inclined by 2.5°. A metallographic examination of the joint was conducted, and there was no defect (e.g., tunnel, lack of fusion, or flying edges) that usually appears in FSW. The high-quality FSW joint had a comparable strength to the base metal. To shorten the sensitization time for the precipitation of the Mg-rich phase, some FSW joints were heat treated at 175 °C for 100 h, followed by air cooling to room temperature.

2.2. Microstructure Characterization

The microstructure characteristics of the through-thickness SZs were examined by electron backscatter diffraction (EBSD). The step size was 1.5 μm. Five samples for EBSD were removed from the SZ and named SZ1–SZ5 from the top to the bottom, respectively (Figure 1a). They were prepared by electro-polishing in a 10% $HClO_4$ + 90% CH_3OH electrolyte at a constant voltage of 15 V for 15–20 s after mechanical grinding and polishing to a surface roughness of 1 µm. An FEI Tecnai F20 transmission electron microscope (TEM) was utilized to characterize the Mg-rich phase along the GBs in sensitized SZs. Three TEM samples were removed from the top (SZ1), middle (SZ3), and bottom (SZ5) of SZ, then ground to a thickness of 100 µm using 2000-grit SiC paper and punched into 3 mm discs. Subsequently, TEM foils were prepared by electro-polishing in a 30% HNO_3 + 70% CH_3OH electrolyte at a voltage of 15 V at −30 °C.

Table 1. Chemical compositions of AA5083-H112 alloy (wt.%).

Material	Si	Fe	Cu	Mn	Mg	Zn	Cr	Ti	Others	Al
AA5083-H112	0.4	0.1	0.1	0.6	4.0	0.2	0.15	0.1	≤0.15	Bal.

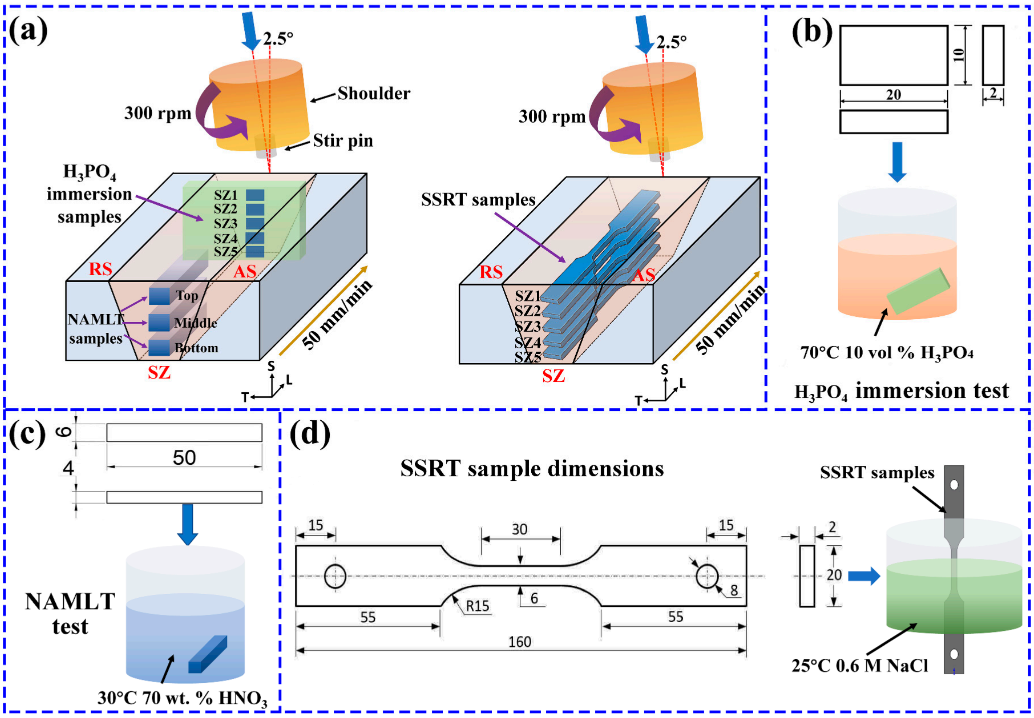

Figure 1. (**a**) Sample locations within the AA5083-H112 FSWed plate. Sample geometries and testing processes of (**b**) H_3PO_4 immersion, (**c**) NAMLT, and (**d**) SSRT.

2.3. Corrosion Testing

The Mg-rich phase at the GB is preferentially corroded when immersed in H_3PO_4 etchant; thus, the distribution of the Mg-rich phase in the sensitized SZs can be indirectly reflected by the identifiable corrosion pits. The sample locations and sizes can be found in Figure 1a,b. Samples were removed from five different through-thickness locations (SZ1–SZ5) and ground to 4000 grid. They were then immersed in 10% H_3PO_4 etchants at 70 °C for 90 s and were subsequently cleaned in alcohol. The corrosion morphologies were examined by a scanning electron microscope (SEM).

The degrees of intergranular corrosion (IGC) susceptibility were also evaluated by the most commonly used nitric acid mass loss testing (NAMLT) according to ASTM G67. The rectangular NAMLT samples with dimensions of 6 mm (L) × 4 mm (S) × 50 mm (L) were removed from the top, middle, and bottom of the SZ (Figure 1a,c). The samples were immersed in a 70 wt.% HNO_3 solution for 24 h at 30 °C. The corroded samples were alcohol-cleaned and blown dry. Duplicate tests for each condition were repeated, and the average values for mass loss were calculated. The corrosion morphologies of the samples after NAMLT were characterized by SEM.

2.4. SSRT Testing

To evaluate the SCC susceptibility of through-thickness SZs, slow strain rate tests (SSRT) of as-welded and sensitized conditions were carried out. The SSRT samples were removed from five individual through-thickness locations (SZ1–SZ5), as shown in Figure 1a,d. The loading axes of these samples were parallel to the welding direction. SSRT samples were loaded in either air or 0.6 M NaCl solution at an initial strain rate of 5×10^{-5} s^{-1}. The SCC susceptibility index (I_{SSRT}) was quantitatively estimated by calculating the percentage loss in the elongations of samples tested in the two environments. The fracture surfaces were observed by SEM subsequently.

3. Results and Discussion

3.1. Microstructures Characterization

The SZ material experienced varying degrees of plastic deformation under the violent shoulder pressing and the pin stirring action, thus resulting in different levels of dynamic recrystallization and the discrepancy in the grain structure throughout the thickness direction. To investigate the correlation between the as-welded grain characteristics and the precipitation of Mg-rich phase after sensitization throughout the thickness, the grain structures of the five individual locations (SZ1 to SZ5) in the SZ were examined by EBSD. Figure 2a–f exhibit the inverse polar figure (IPF) maps of these five samples. All the samples featured dynamic recrystallized grains, sub-grains, and deformed grains. The pre-existing rolled fibrous grains in BM were fully replaced by the fine equiaxed grains, according to the IPFs. The details of the statistical results of grain diameter are displayed in Figure 2g. Generally, the recrystallized grain size exhibited a distinct downward trend from the top to the bottom. Specifically, it was 5.5 ± 3.2 μm for the top of the SZ (SZ1), while it decreased to 3.7 ± 1.9 μm for the bottom of the SZ (SZ5). SZ1 was considered the shoulder affected zone (SAZ). The root diameter of the stir pin was 12.8 mm, and the diameter of the shoulder was up to 26 mm. During the FSW process, this region experienced intense stirring action coupled with forceful pressing from the shoulder, resulting in high frictional heat and deformation energy storage. Thus, the recrystallized grains had sufficient time to grow, and comparatively coarse grains were observed. For the bottom of the SZ (SZ5), however, the small diameter of the stir pin (8 mm for SZ5 vs. 12.8 mm for SZ1) enabled the stirring action to be centralized in a narrow zone. Furthermore, the heat dissipated rapidly through the base metal and the backing plate below the weld. As such, the strong and centralized stirring action, the low welding heat input, and the short heat preservation time synergistically contributed to the relatively fine recrystallized grains at the bottom of the SZ (SZ5).

Figure 3a–e show the dynamic recrystallization distribution of the as-welded SZs. The fractions of recrystallized grain, sub-grain, and deformed grain are exhibited in Figure 3f. The top of the SZ (SZ1) was characterized by the most sub-grains and deformed grains and the lowest fraction of recrystallization grains. In general, the fraction of recrystallized grain presented an upward tendency from SZ1 to SZ5, accompanied by a significant decrease in the fraction of sub-grains, as shown in Figure 3f. It was confirmed that the main mechanism of recrystallization in the SZ is particle-stimulated nucleation (PSN), and the pre-existing second particles (i.e., $Al_6(Mn,Fe)$ and Mg_2Si particles) contributed to the grain refinement in the SZ [34]. The severe stirring action in the lower portion of the SZ can tear up the original large second phase into small particles and make them distribute uniformly. These fine particles can provide nucleation sites for the recrystallized grains. In addition, it is noteworthy that the variations in the degree of dynamic recrystallization exhibited a non-linear trend, and the highest fraction of recrystallized grain was found in the middle to the bottom of the SZ (SZ4) instead of the bottom of the SZ (SZ5). Specifically, SZ4 contained >85% recrystallized grains and less than 15% sub-grains and deformed grains.

This can be rationalized by the following examinations. Previous work demonstrated that the peak temperature decreased while the strain increased from the top to the bottom of the SZ [35]. The backing plate below the weld can facilitate the heat dissipation and increase the cooling rate of the bottom of the SZ. Compared with SZ4, the lower welding heat input and larger plastic deformation in SZ5 were responsible for the lower recrystallized grain fraction in this region. In addition, the top and the bottom of the SZ (SZ1 and SZ5) had similar fractions of deformed grains, higher than those of the other three regions. This phenomenon can be explained by the severe shoulder pressing in SZ1 and the strong stirring action in SZ5 due to the small root diameter of the pin. As mentioned above, the mechanical friction stirring effect of the welding tool was significantly enhanced from the top to the bottom, and this effect became the most pronounced in SZ5. However, it is noteworthy that the top of the SZ still maintained great deformation caused by the severe shoulder pressing, and similar results were confirmed by Imam's work with the aid of DEFORM 3D software (version 11.0) [35]. Hence, both the top and bottom of the SZ (SZ1 and SZ5) preserved high fractions of deformed grains.

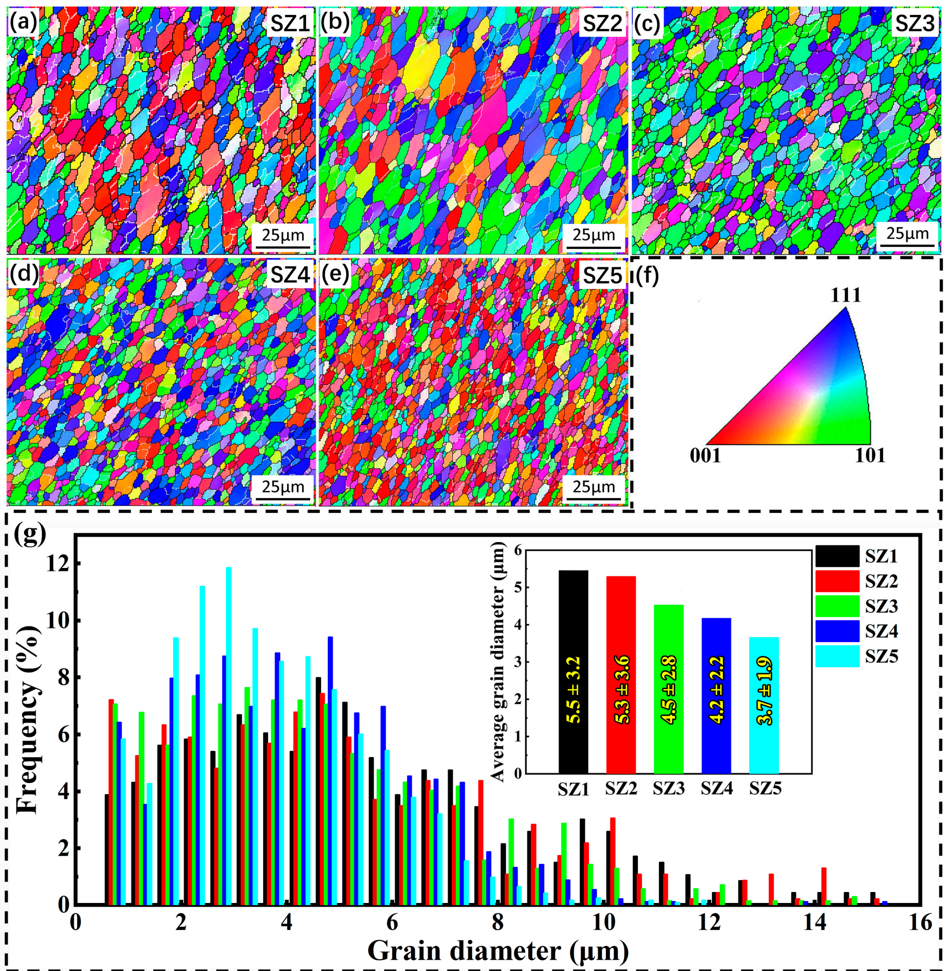

Figure 2. (**a**–**f**) Inverse pole figures of SZ1 to SZ5 (from the top to the bottom) and (**g**) grain size distribution results (the image showing the average grain sizes is inserted).

The density of the low-angle grain boundary (LAGB) can be evaluated as a reflection of the accumulated plastic strain (defined as the misorientation angle lower than 15°). The grain boundary characteristics were further analyzed with the aid of EBSD. Figure 4 presents the results of the grain boundary misorientation of the SZ1 to SZ5 specimens. The fraction of LAGBs demonstrated a significant downward trend and then remained constant. It decreased from 41.6% of SZ1 to 27.6% of SZ4/SZ5. This suggests that the middle to the bottom of the SZ contains a relatively large amount of HAGBs due to the severe plastic deformation induced by the stir pin. These high fractions of HAGBs exhibited in the middle to the bottom of the SZ were also consistent with the high levels of dynamic recrystallization mentioned before, as shown in Figure 3. The grain boundary misorientation significantly affected the Mg-rich phase precipitation behavior during sensitization, which is discussed later.

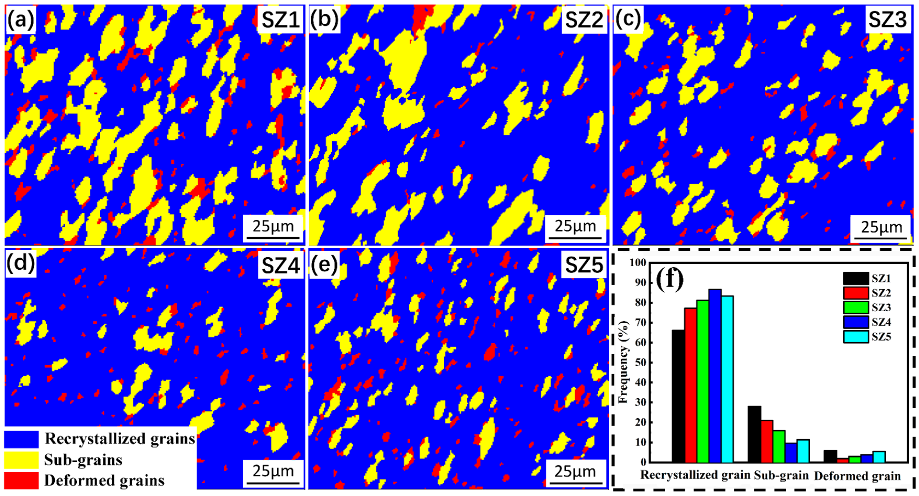

Figure 3. (**a**–**e**) Dynamic recrystallization distribution and (**f**) statistical result of the SZ1–SZ5 EBSD samples.

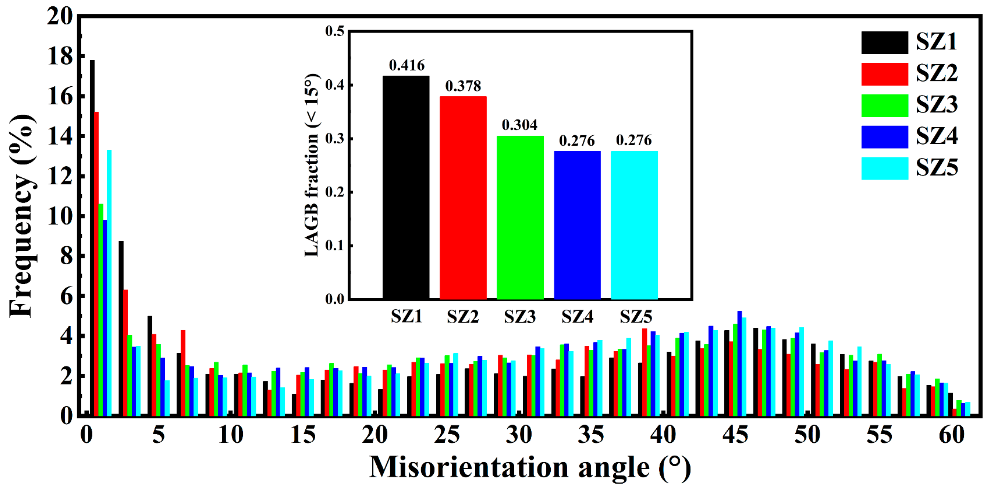

Figure 4. Grain boundary misorientation distribution of SZ1 to SZ5 samples. LAGB fractions are inserted.

To further characterize the variation of the localized storage strain throughout the thickness direction within the SZ, kernel average misorientation (KAM) maps were employed by calculating the average degree within the set of all the neighboring misorientations. Figure 5a–f present the KAM maps of the SZs, from SZ1 to SZ5, and the KAM statistics results are shown in Figure 5g. The large average local misorientations exhibited in the top (0.556° for SZ1) and bottom (0.552° for SZ5) indicate the significant accumulated local plastic stain and high levels of dislocation density in these regions. SZ2, SZ3, and SZ4 possessed similar degrees of strain storage, and the average local misorientation reached 0.445°, 0.447°, and 0.462°, respectively. The greater degrees of storage stain within SZ1 and SZ5 were primarily a consequence of more aggressive plastic deformation and more dislocation generation and convergence induced by the shoulder and stir pin. These results correlate well with the aforementioned dynamic recrystallization analysis, which suggests that SZ1 and SZ5 contained larger amounts of the deformed grains.

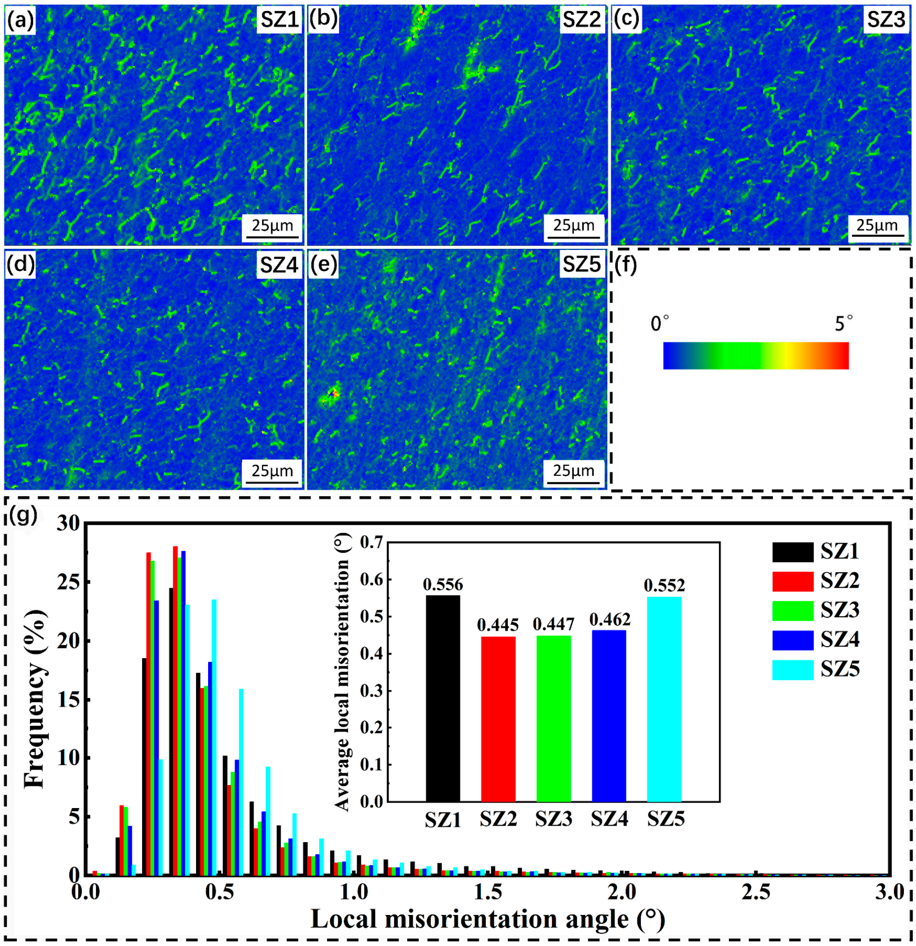

Figure 5. (**a**–**f**) KAM maps of the SZ1–SZ5 samples and (**g**) KAM statistical results with an inserted image showing the average local misorientation values.

Summarizing the EBSD results mentioned above, significant microstructure difference throughout the thickness of the SZ was presented as a result of the non-uniform heat and plastic deformation distributions during the FSW process. The SZs of the FSWed thick plate experienced the typical dynamic recrystallization process. From SZ1 to SZ5, significant decreases in the grain size and the LAGB fraction were identified. Interestingly, the degree of recrystallization increased from the top to the bottom of the SZ, and the highest fraction of recrystallized grains was observed in SZ4. Correspondingly, greater fractions of HAGB were exhibited in the SZ4 and SZ5 regions. In addition, the KAM work herein suggests that the top (SZ1) and the bottom (SZ5) of the SZ preserved more accumulated strain and dislocation density than the other three regions. The higher fractions of the deformed grains within SZ1 and SZ5 can be attributed to the greater levels of plastic deformation induced by the shoulder pressing and the stirring action of the pin in these two regions.

The through-thickness microstructural characteristics mentioned above play an important role in the Mg-rich phase precipitation behavior during sensitization. Figure 6 presents the typical TEM images showing the Mg-rich precipitates along GBs in the top, middle, and bottom of 175 °C/100 h sensitized SZ (SZ1, SZ3, and SZ5, respectively). The fragmentations of the primitive intermetallic particles were apparently observed in the SZ, induced by the severe rotation action of the stir pin during the FSW process. The rod-shaped pre-existing particles are hypothetically assumed to be Al_6(Mn-Fe-Cr-Si) or Mg_2Si, as proven by our previous work [29]. As expected, a large number of dislocation entanglements was present in the matrix or intersecting with the GBs or the pre-existing particles. These dislocations are in accordance with the previous KAM results (Figure 5). The Mg-rich phase along the GBs in the different regions of the SZ exhibited similar precipitation behaviors. The GBs were decorated by discontinuous Mg-rich precipitates, especially at the triple junction, with dislocations surrounded, as seen in Figure 6c–f. Simultaneously, only a small amount of Mg-rich phase precipitate adjacent to the fragmented second-phase particles. The thickness of Mg-rich precipitate along the GB was about 100 nm for all the regions of the SZ. The middle and bottom samples appeared to exhibit slightly more Mg-rich phase than the top sample. This difference was, however, not significant. The selected area electron diffraction (SAED) analysis of the Mg-rich precipitate at the triple junction is inserted in Figure 6f. It suggests that β′-Al_3Mg_2 phase with hexagonal close-packed (HCP) structure precipitated in the sensitized SZ. The electrochemically active β′ phase can preferentially dissolve in corrosive environments and dramatically deteriorate the IGC/SCC resistance.

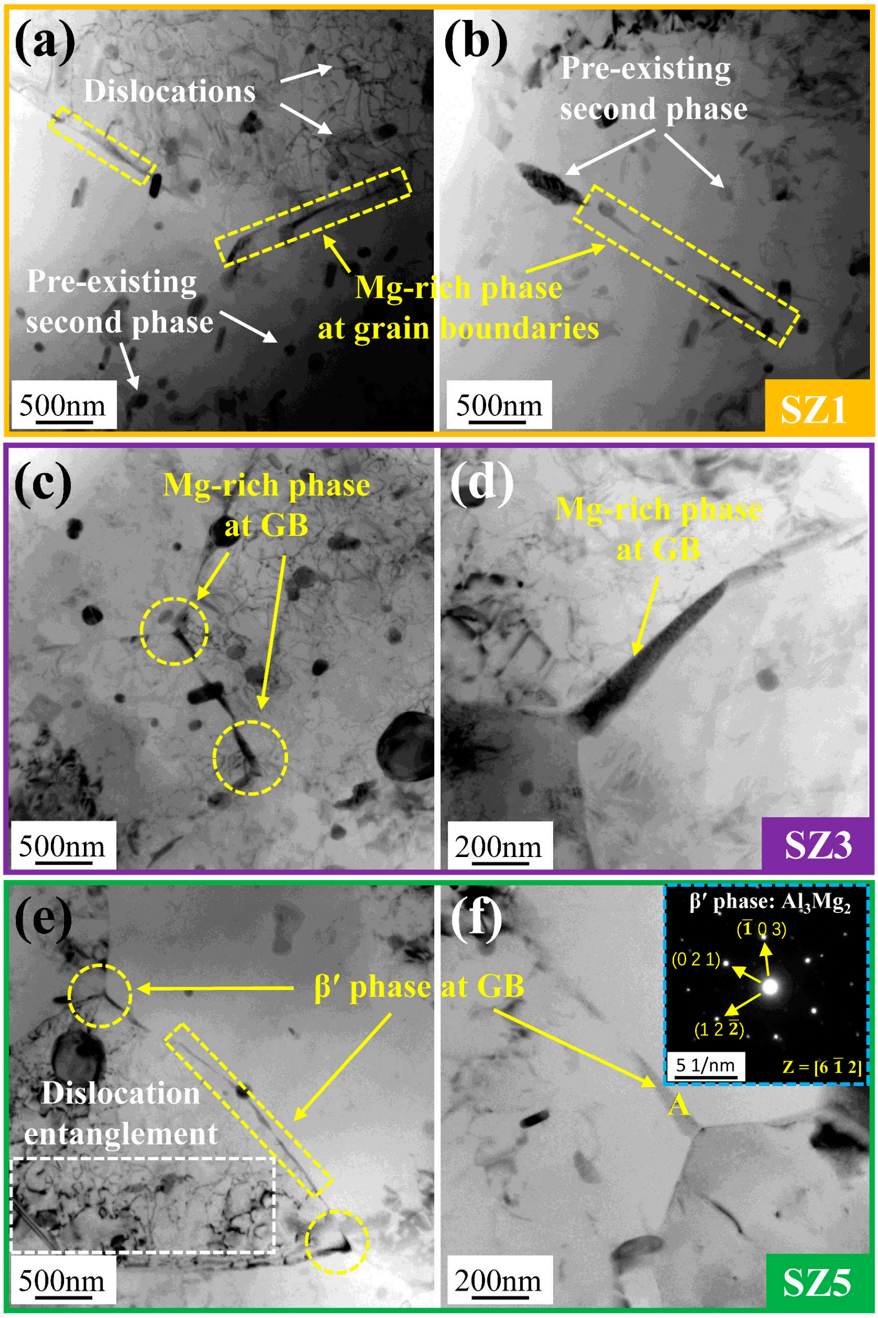

Figure 6. TEM bright field images of 175 °C/100 h sensitized (**a**,**b**) SZ1, (**c**,**d**) SZ3, and (**e**,**f**) SZ5 samples. Typical SAED analysis of the β′-Al_3Mg_2 phase along GB (marked by yellow 'A' in Figure 6f), is inserted in Figure 6f.

3.2. H_3PO_4 Etchant Immersion Tests

Mg-rich precipitates are more vulnerable to the weak corrosive H_3PO_4 etchant compared with the matrix. Hence, the distribution and continuity of Mg-rich phase before immersion can be indirectly characterized by the etched grain boundaries or the corrosion pits. Figure 7 presents the corroded surface morphologies of the through-thickness sensitized SZs after exposure to 10 vol% H_3PO_4 etchant. For all the SZs, the grain boundaries were visibly etched, accompanied by a few corrosion pits, indicating that Mg-rich precipitates preferentially nucleated and grew along the GBs owing to the low activation energy barrier herein. The etched GBs clearly revealed the grain morphologies and indicated that the grain size decreased gradually from the top to the bottom of the SZ, consistent with the EBSD results in Figure 2. Notably, the middle to the bottom of SZs (SZ4 and SZ5) exhibited more continuous corrosion pits along the GBs, while the top of the SZs (SZ1 and SZ2) possessed comparatively discrete and discontinuous Mg-rich phase. The quantitative analysis of the pit distribution was achieved by Image J software (version 1.54d) by calculating the ratio of the total pixels of the pits to the total pixels of the image. A series of image recognition processing methods, such as "Find edges" and "Threshold", was performed using Image J prior to the statistical calculation. It was found that the proportion of the pit area increased with the decreasing grain size from SZ1 to SZ5. Specifically, they were 9.07%, 10.67%, 12.72%, 14.09%, and 15.26% for SZ1, SZ2, SZ3, SZ4, and SZ5, respectively. This phenomenon can be explained by the grain boundary fraction and the grain size. Finer grains mean more GB fraction and more nucleation sites for the Mg-rich phase. As a result, the lower part of the sensitized SZ exhibited more corrosion attacks than the upper part. The H_3PO_4 immersion test results herein suggest that the GBs of the sensitized SZs exhibit apparent IGC susceptibility, especially in the lower part. Further IGC evidence was provided by the NAMLT tests, as shown below.

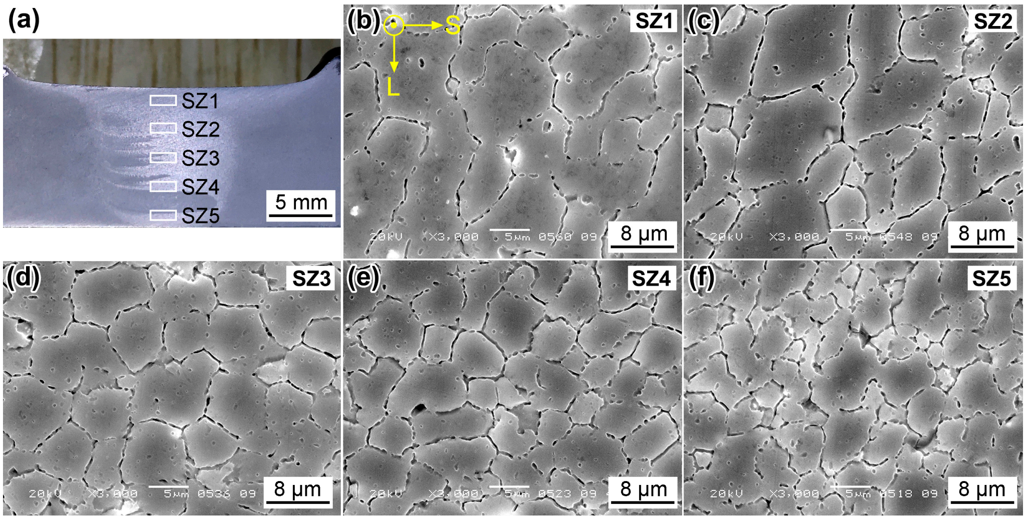

Figure 7. (**a**) Sample locations of H_3PO_4 etchant immersion tests; (**b**–**f**) SEM images of the corroded surfaces after the immersion tests of 175 °C/100 h sensitized SZ.

3.3. NAMLT Tests

To further analyze the IGC tendency of the as-welded and sensitized SZ, NAMLT was employed by calculating the mass loss value and checking the corroded morphologies. A value lower than 15 mg/cm^2 was considered excellent resistance to IGC based on ASTM G67. NAMLT samples were removed from three locations (the top, middle, and bottom of the SZ), as shown in Figure 1a. Figure 8 exhibits the NAMLT results of the as-welded and the sensitized SZ samples. The NAMLT values of all the as-welded samples maintained a low level (<5 mg/cm^2), suggesting superior IGC resistance. Similar results were also found in previous research [36]. For the 175 °C/100 h sensitized samples, the NAMLT values increased sharply, indicating a pronounced IGC susceptibility. The NAMLT value increased from 2.46–4.62 mg/cm^2 for the as-welded samples to 65.73–76.39 mg/cm^2 for the sensitized samples. Notably, larger NAMLT values were obtained for the sensitized middle and bottom samples, further indicating a high number of β′ precipitates at the GBs within these two regions. This finding is also consistent with the H_3PO_4 immersion morphologies, as seen in Figure 7. The large IGC tendency exhibited in the sensitized middle and bottom samples can be rationalized by the following explanations. The Mg-rich precipitates along GB of the top SZ distributed less continuously than those of the middle and bottom samples (Figure 7). The GBs free of the Mg-rich phase enabled the top SZ to be less susceptible to IGC by hindering the anodic dissolution and the IGC propagation. The increasing tendency to IGC from the top to the bottom could be ascribed to the progressively increasing grain refinement and continuity of the Mg-rich precipitates. Refined grains are more prone to detach in an aggressive concentrated nitric acid solution. As such, the middle and bottom samples of the sensitized SZ exhibited a slightly larger IGC tendency than the top sample.

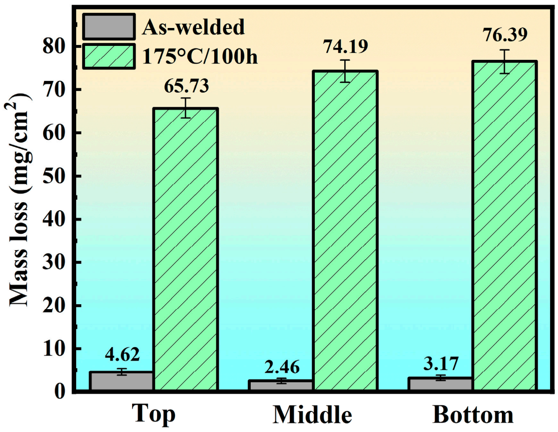

Figure 8. Mass loss values of the SZ samples after NAMLT.

The corrosion morphologies of as-welded and sensitized SZ3 after NAMLT are displayed in Figure 9. The variation in the corrosion morphology of the through-thickness SZs is not clearly distinguishable; thus, only the corroded surfaces of the middle samples are shown in Figure 9. For the as-welded SZ3, the etched surface is flat and smooth. Only a slight amount of grain fall-out with limited pitting attack was observed, as evidenced by the extremely low NAMLT value (Figure 8). Conversely, the 175 °C/100 h sensitized SZ presented a rough corroded surface characterized by apparent IGC morphology. A large amount of corrosion attacks and grain fall-out were observed, leaving visible island-shaped corroded grains and deep corrosion trenches behind. These unique corrosion morphologies were triggered by the anodic dissolution of the GBs decorated by the relatively continuous Mg-rich phase with high electro-chemical activity. Our previous studies provided evidence that the grain morphology (e.g., shape and size) strongly affects the IGC tendency [29]. Although NAMLT values indicate that the samples removed from the middle and bottom of the SZ exhibited weaker IGC resistance than those removed from the top, little difference in the corrosion morphology could be detected. This is primarily attributed to the small difference in the grain morphology of the SZs throughout the thickness direction. Recrystallized refined grains were produced in all the regions of SZ. Notwithstanding the decrease in the grain size from the top to the bottom of SZ, it does not play a leading role in the corrosion attack when immersed in an aggressive nitric acid solution. The NAMLT values and IGC tendency are strongly correlated with SCC behavior, as discussed subsequently.

3.4. Slow Strain Rate Tests

Figure 10 shows the SSRT curves of the 175 °C/100 h sensitized SZs at an initial strain rate of 1×10^{-5} s^{-1}. The excellent SCC immunity in the as-welded SZ was quantitatively confirmed by the stress vs. strain curves and the fracture morphologies in our previous work [29]; thus, only the SSRT results of sensitized SZs are exhibited herein. The yield stress

(YS), ultimate tensile strength (UTS), elongation, and SCC susceptibility indices (I_{SSRT}) are summarized in Table 2. When tested in lab air, all the sensitized SZs still maintained high elongations (>28%), albeit the large number of Mg-rich precipitates along the GBs (Figure 6). Compared with the top SZs (SZ1 and SZ2), higher YS and UTS were found in the middle to bottom of the SZs (SZ3, SZ4, and SZ5), primarily as a consequence of the through-thickness grain refinement strengthening from the top to the bottom (Figure 2). These results suggest that the Mg-rich phase along the GB has no distinct effect on GB weakening and tensile properties when tested in a non-aggressive environment. Conversely, the SZs became extremely vulnerable to SCC when tested in 0.6 M NaCl solution, as reflected by the large drop of the stress–strain curves and the low elongations. Considerable reductions in UTS and elongations were observed in all the samples. Moreover, the middle and bottom of the SZs appeared to manifest a slightly more pronounced susceptibility to SCC, as evidenced by comparatively greater I_{SSRT} (68.6–73.1%) than that of the top samples. These results demonstrate that the lower portion of the SZ evinces a more prominent SCC tendency after 175 °C/100 h sensitization, despite its superior mechanical properties under the as-welded condition.

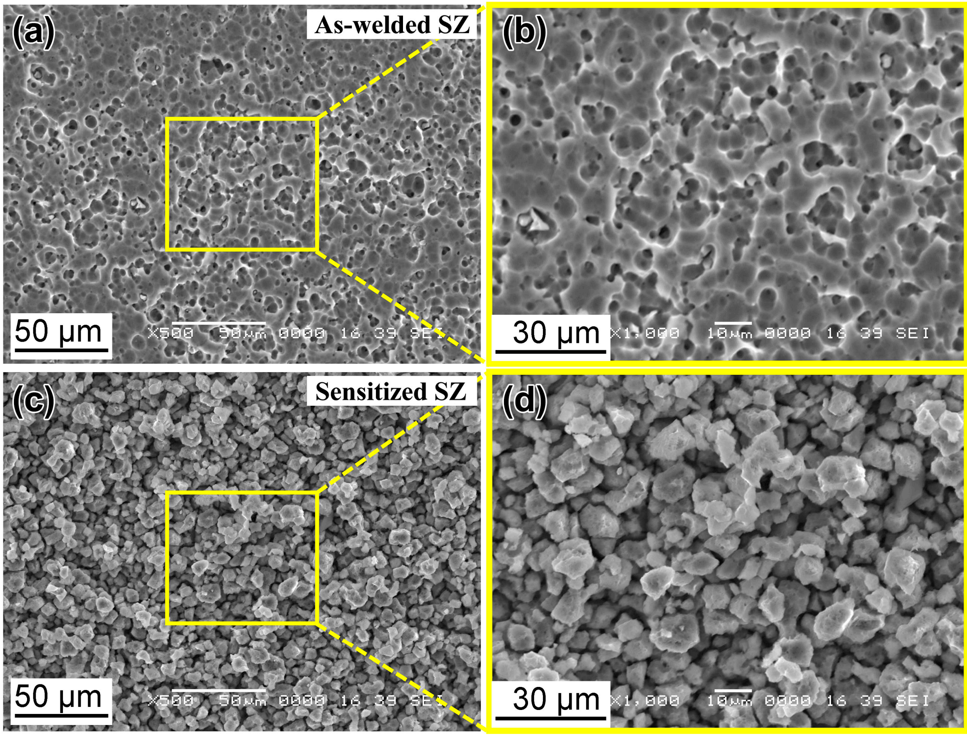

Figure 9. SEM images showing corrosion morphologies of (**a**,**b**) as-welded and (**c**,**d**) 175 °C/100 h sensitized SZ3 after NAMLT.

While the test environment did not influence the yield strength, the samples tested in NaCl solution exhibited much lower UTS and elongations than those of the samples tested in lab air. This can be explained by the interaction of the tensile stress and the β' phase dissolution. At a low stress level, the tensile stress is not high enough to promote the anodic dissolution or drive SCC propagation. As a result, similar yield strengths were found in the samples tested in the two environments. At a high stress level, on the contrary, tensile stress can lead to the stress concentration and facilitate the anodic dissolution, thus accelerating SCC propagation. This led to the large reduction in UTS and elongation.

It should be noted that the tensile curves of the samples tested in lab air exhibited serrated stress–strain responses at large strains, which was reported in our previous paper and is called the PLC effect [5]. The PLC phenomenon is associated with the interactions between the dynamic solute atoms and dislocations. The dislocation motion can be hindered by the solute atoms and leads to the work hardening. Once the dislocations bypass the solute atoms, there might be an abrupt softening in the sample, and a sudden drop is present in the tensile curve. However, PLC effects were not exhibited in the samples tested in the NaCl solution. The absence of the PLC effect can be explained by the weak solute atom dislocation interactions at low tensile stress for these samples. The interactions were not strong enough to promote distinct serrations in the stress–stain curves.

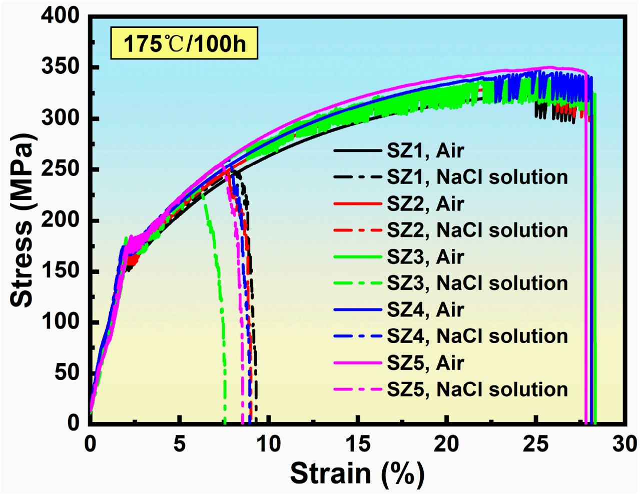

Figure 10. SSRT curves of the 175 °C/100 h sensitized SZ samples.

Table 2. Summary of SSRT results of the 175 °C/100 h sensitized SZ samples.

Location	Test Environment	YS (MPa)	UTS (MPa)	Elongation (%)	I_{SSRT} (%)
SZ1	Air 0.6 M NaCl	160 161	344 263	28.1 9.3	66.9
SZ2	Air 0.6 M NaCl	161 163	339 257	28.2 9.0	68.1
SZ3	Air 0.6 M NaCl	172 170	339 230	28.3 7.6	73.1
SZ4	Air 0.6 M NaCl	172 170	345 259	28.2 8.7	69.1
SZ5	Air 0.6 M NaCl	179 172	352 254	28.0 8.8	68.6

Figure 11 exhibits the fractography of the 175 °C/100 h sensitized SZs tested in NaCl solution. All the surfaces of the through-thickness SZ samples manifested themselves as a plethora of typical flat intergranular (IG) features with corrosion products covered at the edges of the samples. Refined recrystallized grains were visible in the IG regions due to the dissolution of GB Mg-rich precipitates. These fractography features are consistent with the large SCC susceptibility index, as seen in Table 2. Some ductile transgranular fracture characteristics (e.g., dimples or tear ridges) were observed in the regions away from the crack source. Notably, the SZ3, SZ4, and SZ5 samples exhibited more visible corrosion product coverage and flat IG features, as seen in Figure 11c–e. These significant IG features, accompanied by the great SCC susceptibility index (I_{SSRT}), indicate the extremely large SCC tendency in all the through-thickness locations of the SZ, especially in the middle to bottom SZ samples (SZ3-5).

The SSRT results herein correlate well with the H_3PO_4 etchant immersion tests and the NAMLT tests. The middle to the bottom of SZs (SZ3, SZ4, and SZ5) exhibited larger IGC/SCC susceptibility than the top SZs (SZ1 and SZ2). These findings can be rationalized by the SCC mechanism of sensitized Al-Mg alloys. The SCC mechanism, i.e., the anodic dissolution of Mg-rich phase and hydrogen embrittlement, has been well established and accepted [20–24]. Although 100 nm thick β′-Al_3Mg_2 phase is found to precipitate in all the SZ regions, the middle to the bottom SZs appeared to possess more continuous precipitates than the top SZ, as confirmed by TEM (Figure 6) and immersion tests (Figure 7). The grain refinement in the lower part of SZ could have facilitated the precipitation of β'-Al_3Mg_2 phase, and thus the dissolution of β' phase could provide the crack path for IGC or SCC. Also, more β' phase could accelerate the acidification of the crack tip solution and promote the anodic dissolution and hydrogen embrittlement within the plastic zone of the crack tip. The effect of β' phase on SCC is more pronounced when the grain size decreases. Furthermore, grain refinement could promote SCC due to the less tortuous SCC propagation path and crack deflections. In sum, the large IGC/SCC tendency exhibited in the lower part of sensitized SZ could be attributed to the more continuous β'-Al_3Mg_2 phase distribution and the grain refinement in these regions.

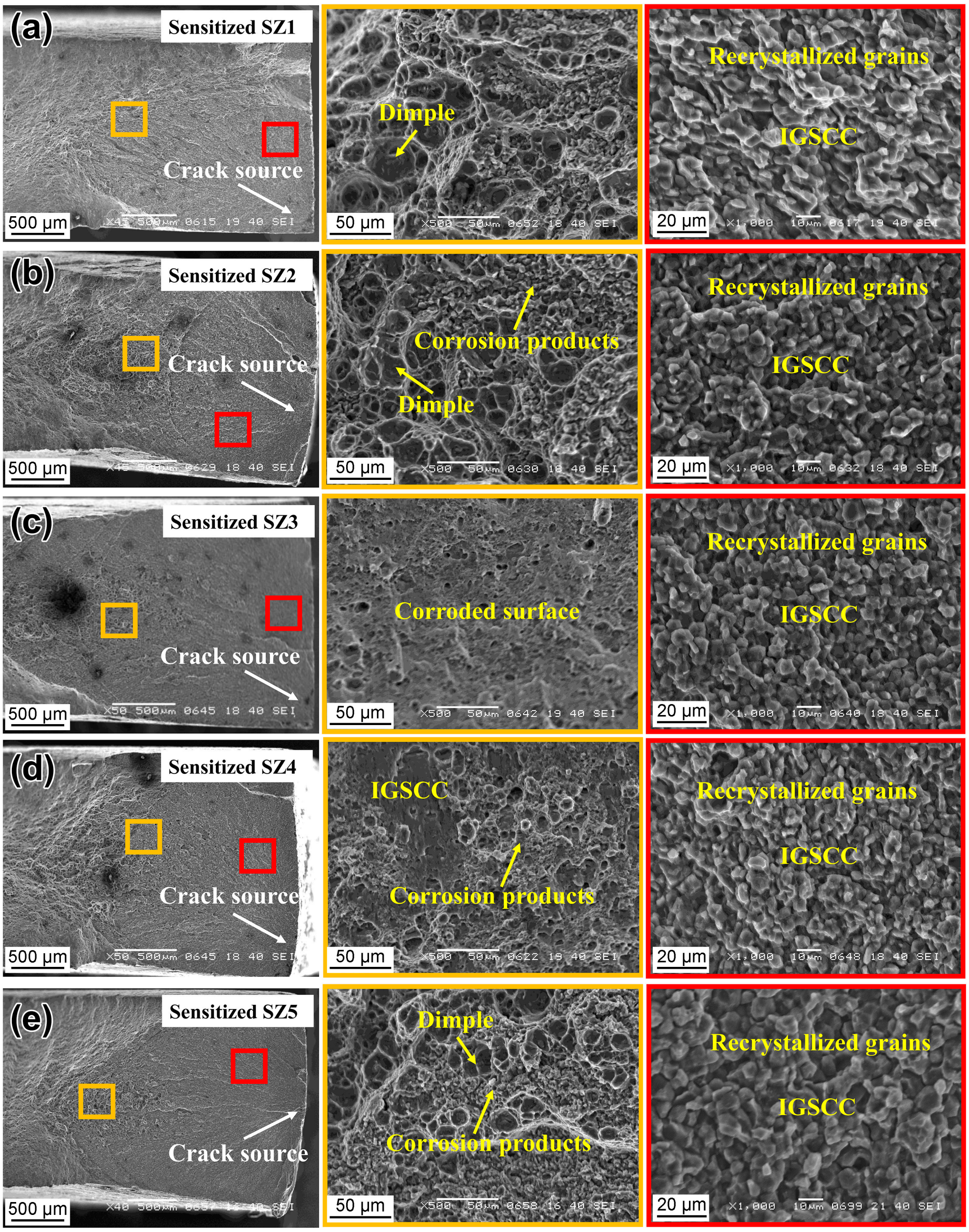

Figure 11. (**a**–**e**) SEM fracture images of 175 °C/100 h sensitized SZ1–SZ5 samples tested in 0.6 M NaCl solution, respectively. High-magnification images with red or yellow borders are from the corresponding red or yellow boxes.

It should be noted that the present work did not involve the effect of welding residual stress on the SCC behavior. Previous work showed that the maximum tensile residual stress was in the range of 40~60 MPa for the 3 mm AA5083 FSW joint [37]. Moreover, the residual stress could release during sample processing due to the decrease in the material constraint. However, large residual stress might exist in the thick aluminum FSW joint, and it should not be ignored in the investigation of the sensitization and SCC susceptibility. As a result, the applied stress exerted on the SSRT sample is, in fact, a combination of the residual tensile stress and the actual applied stress. An accurate measurement of the residual stress distribution should be conducted, especially for the thick plate. This was out of the scope of the present work, and much effort should be made in the future.

4. Conclusions

The present study investigated the inhomogeneity of the Mg-rich phase precipitation behavior and the corrosion resistance throughout the thickness direction of SZ. The major conclusions are as follows:

1. The grain size of the SZ progressively decreased from the top to the bottom. The strong and centralized stirring action and the heat dissipation due to the backing plate contributed to the relatively fine recrystallized grains at the bottom of the SZ (SZ5).
2. There was an upward trend in the degree of dynamic recrystallization from the top to the bottom of the SZ. However, the highest fraction was found in the SZ4 region, instead of the bottom of SZ (SZ5). Compared with SZ4, the lower welding heat input and the larger plastic deformation in SZ5 were responsible for the lower recrystallized grain fraction in this region.
3. Higher levels of deformed grains were observed in the top (SZ1) and bottom of SZ (SZ5), and this can be attributed to the greater levels of plastic deformation induced by the shoulder pressing and the strong stirring action of the pin in these two regions, respectively.
4. A 100-nm-thick β'-Al_3Mg_2 phase was found to precipitate along the grain boundaries in all the SZ samples. The middle and bottom of the SZ exhibited more continuous precipitates along the GBs due to the finer grain size and the larger fraction of HAGBs in these regions.
5. Although all the as-welded samples removed from the SZ exhibited excellent corrosion resistance, they became extremely susceptible to IGC and SCC after sensitization. The middle to the bottom of the SZ samples possessed a slightly greater IGC/SCC tendency compared with the top sample.

Author Contributions: Conceptualization, W.G.; methodology, L.C. and W.L.; software, J.N.; validation, X.G., W.L. and H.L.; formal analysis, X.G.; investigation, J.N.; data curation, J.N.; writing—original draft preparation, J.N.; writing—review and editing, W.G., L.C. and J.J.L.; visualization, X.G.; funding acquisition, W.G., X.G. and J.J.L. All authors have read and agreed to the published version of the manuscript.

Funding: This research was funded by the National Natural Science Foundation of China (52375339, 51705218), the Fundamental Research Program of Jiangsu Province (BK20201000), the Basic and Applied Basic Research Foundation of Guangdong Province (2021A1515110729), the Foshan (Southern China) Institute for New Materials (2021AYF25017), and the financial support of ONR-N000014-17-1-2573.

Data Availability Statement: The data supporting this study's findings are available from the corresponding author upon reasonable request.

Conflicts of Interest: The authors declare that they have no known competing financial interest or personal relationships that could have appeared to influence the work reported in this paper.

References

1. Chen, Q.; Xie, Z.; Wang, J.; Lin, S.; Dou, Q.; Huang, T. A comparison of the swing and non-swing arc behavior in arc ultrasonic assisted narrow gap GMAW. *J. Mater. Res. Technol.* **2023**, *24*, 4698–4710. [CrossRef]
2. Wang, L.; Wu, T.; Wang, D.; Liang, Z.; Yang, X.; Peng, Z.; Liu, Y.; Liang, Y.; Zeng, Z.; Oliveira, J.P. A novel heterogeneous multi-wire indirect arc directed energy deposition for in-situ synthesis Al-Zn-Mg-Cu alloy: Process, microstructure and mechanical properties. *Addit. Manuf.* **2023**, *72*, 103639. [CrossRef]
3. Gao, W.; Gu, Y.; Chen, L.; Liang, H.; Wang, D.; Seifi, M.; Lewandowski, J.J. Effects of sensitization on environmentally assisted cracking of AA5083-H128 Al–Mg alloy. *J. Mater. Res. Technol.* **2023**, *25*, 681–697. [CrossRef]
4. Xu, G.; Li, L.; Wang, H.; Li, P.; Guo, Q.; Hu, Q.; Du, B. Simulation and experimental studies of keyhole induced porosity in laser-MIG hybrid fillet welding of aluminum alloy in the horizontal position. *Opt. Laser Technol.* **2019**, *119*, 105667. [CrossRef]
5. Gao, W.; Wang, D.; Seifi, M.; Lewandowski, J.J. Anisotropy of corrosion and environmental cracking in AA5083-H128 Al-Mg alloy. *Mater. Sci. Eng. A* **2018**, *730*, 367–379. [CrossRef]
6. Golumbfskie, W.J.; Tran, K.T.; Noland, J.M.; Park, R.; Stiles, D.J.; Grogan, G.; Wong, C. Survey of detection, mitigation, and repair technologies to address problems caused by sensitization of Al-Mg alloys on navy ships. *Corrosion* **2016**, *72*, 314–328. [CrossRef] [PubMed]
7. Lyndon, J.A.; Gupta, R.K.; Gibson, M.A.; Birbilis, N. Electrochemical behaviour of the β-phase intermetallic (Mg_2Al_3) as a function of pH as relevant to corrosion of aluminium–magnesium alloys. *Corros. Sci.* **2013**, *70*, 290–293. [CrossRef]
8. Zhang, R.; Knight, S.P.; Holtz, R.L.; Goswami, R.; Davies, C.H.J.; Birbilis, N. A survey of sensitization in 5xxx series aluminum alloys. *Corrosion* **2016**, *72*, 144–159. [CrossRef]
9. D′Antuono, D.S.; Gaies, J.; Golumbfskie, W.; Taheri, M.L. Direct measurement of the effect of cold rolling on β phase precipitation kinetics in 5xxx series aluminum alloys. *Acta Mater.* **2017**, *123*, 264–271.
10. Birbilis, N. The influence of grain size and grain orientation on sensitisation in AA5083. *Corrosion* **2015**, *72*, 160–168. [CrossRef]
11. Zhu, Y.; Cullen, D.A.; Kar, S.; Free, M.L.; Allard, L.F. Evaluation of Al_3Mg_2 precipitates and Mn-rich phase in aluminum-magnesium alloy based on scanning transmission electron microscopy imaging. *Metall. Mater. Trans. A* **2012**, *43*, 4933–4939. [CrossRef]
12. Goswami, R.; Holtz, R.L. Transmission electron microscopic investigations of grain boundary beta phase precipitation in Al 5083 aged at 373 K (100 °C). *Metall. Mater. Trans. A* **2013**, *44*, 1279–1289. [CrossRef]
13. D'Antuono, D.S.; Gaies, J.; Golumbfskie, W.; Taheri, M. Grain boundary misorientation dependence ofβ phase precipitation in an Al–Mg alloy. *Scr. Mater.* **2014**, *76*, 81–84. [CrossRef]
14. Zhao, Y.; Mikhail, N.P.; Matthew, M.; Michael, E.K.; Andrea, M.H. The role of grain boundary plane orientation in the β phase precipitation of an Al-Mg alloy. *Scr. Mater.* **2014**, *89*, 49–52. [CrossRef]
15. Golovin, I.S.; Mikhaylovskaya, A.V.; Sinning, H.R. Role of the β-phase in grain boundary and dislocation anelasticity in binary Al-Mg alloys. *J. Alloys Compd.* **2013**, *577*, 622–632. [CrossRef]
16. Gary, S.W.; Diana, F.; Ian, M.R. Micromechanics of dislocation channeling in intergranular stress corrosion crack nucleation. *Curr. Opin. Solid. State. Mater. Sci.* **2012**, *16*, 134–142.
17. Yi, G.; Littrell, K.C.; Poplawsky, J.D.; Cullen, D.A.; Sundberg, E.; Free, M.L. Characterization of the effects of different tempers and aging temperatures on the precipitation behavior of Al-Mg (5.25 at.%)-Mn alloys. *Mater. Des.* **2017**, *118*, 22–35. [CrossRef]
18. Tayyebi, M.; Adhami, M.; Karimi, A.; Rahmatabadi, D.; Alizadeh, M.; Hashemi, R. Effects of strain accumulation and annealing on interfacial microstructure and grain structure (Mg and Al_3Mg_2 layers) of Al/Cu/Mg multilayered composite fabricated by ARB process. *J. Mater. Res. Technol.* **2021**, *14*, 392–406. [CrossRef]
19. Chen, W.; Hou, H.; Zhang, Y.; Liu, W.; Zhao, Y. Thermal and solute diffusion in a-Mg dendrite growth of Mg-5wt.%Zn alloy: A phase-field study. *J. Mater. Res. Technol.* **2023**, *24*, 8401–8413. [CrossRef]
20. Daniel, L.F.; Asher, C.L.; Andrew, C.L.; Mitra, L.T. Evolution of β-phase precipitates in an aluminum-magnesium alloy at the nanoscale. *Acta Mater.* **2020**, *185*, 279–286.
21. Sauvage, X.; Enikeev, N.; Valiev, R.; Nasedkina, Y.; Murashkin, M. Atomic-scale analysis of the segregation and precipitation mechanisms in a severely deformed Al–Mg alloy. *Acta Mater.* **2014**, *72*, 125–136. [CrossRef]
22. Hirayama, K.; Toda, H.; Fu, D.; Masunaga, R.; Su, H.; Shimizu, K.; Akihisa, T.; Masayuki, U. Damage micromechanisms of stress corrosion cracking in Al-Mg alloy with high magnesium content. *Corros. Sci.* **2021**, *184*, 109343–109349. [CrossRef]
23. Lim, M.L.C.; Kelly, R.G.; Scully, J.R. Overview of intergranular corrosion mechanisms, phenomenological observations, and modeling of AA5083. *Corrosion* **2015**, *72*, 198–220. [CrossRef] [PubMed]
24. Seifi, M.; Ghamarian, I.; Samimi, P.; Collins, P.C.; Holroyd, N.J.H.; Lewandowski, J.J. Sensitization and remediation effects on environmentally assisted cracking of Al-Mg naval alloys. *Corros. Sci.* **2018**, *138*, 219–241. [CrossRef]
25. Du, C.; Pan, Q.; Chen, S.; Tian, S. Effect of rolling on the microstructure and mechanical properties of 6061-T6 DS-FSW plate. *Mater. Sci. Eng. A* **2020**, *772*, 138692–138704. [CrossRef]
26. Malopheyev, S.; Kulitskiy, V.; Mironov, S.; Zhemchuzhnikova, D.; Kaibyshev, R. Friction-stir welding of an Al–Mg–Sc–Zr alloy in as-fabricated and work-hardened conditions. *Mater. Sci. Eng. A* **2014**, *600*, 159–170. [CrossRef]
27. Li, Y.; Xia, W.; Yan, H.; Chen, J.; Ding, T.; Sun, Y.; Li, X. Microstructure and mechanical properties of friction-stir-welded high-Mg-alloyed Al-Mg alloy plates at different rotating rates. *Rare Met.* **2021**, *40*, 2167–2178. [CrossRef]

28. Vysotskiy, I.; Zhemchuzhnikova, D.; Malopheyev, S.; Mironov, S.; Kaibyshev, R. Microstructure evolution and strengthening mechanisms in friction-stir welded Al-Mg-Sc alloy. *Mater. Sci. Eng. A* **2020**, *770*, 138540–138548. [CrossRef]
29. Ning, J.; Gao, W.; Gu, X.; Zhang, H.; Guan, W.; Li, W.; Liang, H.; Wang, D.; Lewandowski, J.J. Precipitation behavior and corrosion properties of friction stir welded AA5083 Al Mg alloy after sensitization. *Mater. Charact.* **2023**, *199*, 112782–112797. [CrossRef]
30. Sen, M.; Puri, A.B. Formation of intermetallic compounds (IMCs) in FSW of aluminum and magnesium alloys (Al/Mg alloys)—A review. *Mater. Today Commun.* **2022**, *33*, 105017–105037. [CrossRef]
31. Qiu, Y.; Yang, X.; Xu, J.; Li, J.; Xiang, S.; Chen, Z.; Sanders, R.E. Enhanced mechanical property and corrosion resistance of alloy 5182 FSW joints by Sc and Zr alloying. *Mater. Charact.* **2022**, *194*, 112412–112422. [CrossRef]
32. Choi, D.H.; Ahn, B.W.; David, J.Q.; Jung, S.B. Behavior of β phase (Al_3Mg_2) in AA 5083 during friction stir welding. *Intermetallics* **2013**, *35*, 120–127. [CrossRef]
33. Gao, W.; Wang, D.; Seifi, M.; Lewandowski, J.J. Through-thickness inhomogeneity of environmentally assisted cracking (EAC) in AA5083-H128 alloy. *Mater. Sci. Eng. A* **2019**, *740*, 34–48. [CrossRef]
34. Imam, M.; Sun, Y.; Fuji, H.; Ma, N.S.; Tsutsumi, S.; Murakawa, H. Microstructural characteristics and mechanical properties of friction stir welded thick 5083 aluminum alloy. *Metall. Mater. Trans. A* **2017**, *48*, 208–229. [CrossRef]
35. Imam, M.; Sun, Y.; Fuji, H.; Ma, N.S.; Tsutsumi, S.; Ahmed, S.J.; Chintapenta, V.; Murakawa, H. Deformation characteristics and microstructural evolution in friction stir welding of thick 5083 aluminum alloy. *Int. J. Adv. Manuf. Technol.* **2018**, *99*, 663–681. [CrossRef]
36. Guo, N.; Fu, Y.; Wang, Y.; Meng, Q.; Zhu, Y. Microstructure and mechanical properties in friction stir welded 5A06 aluminum alloy thick plate. *Mater. Des.* **2017**, *113*, 273–283. [CrossRef]
37. Peel, M.; Steuwer, A.; Preuss, M.; Withers, P.J. Microstructure, mechanical properties and residual stresses as a function of welding speed in aluminium AA5083 friction stir welds. *Acta Mater.* **2003**, *51*, 4791–4801. [CrossRef]